Additive Manufacturing 42 (2021) 101961

Contents lists available at ScienceDirect

Additive Manufacturing

journal homepage: www.elsevier.com/locate/addma

Research Paper

Deep representation learning for process variation management in laser powder bed fusion

Sepehr Fathizadan [a], Feng Ju [a,*], Yan Lu [b,1]

[a] School of Computing, Informatics, and Decision Systems Engineering, Arizona State University, Tempe, AZ 85281 USA
[b] National Institute of Standard and Technology, Engineering Laboratory, Gaithersburg, MD 20899, USA

ARTICLE INFO

Keywords:
Laser powder bed fusion
Additive manufacturing
Melt pool image
Deep learning
Anomaly detection

ABSTRACT

Laser Powder Bed Fusion (LPBF) is an additive manufacturing process where laser power is applied to fuse the spread powder and fabricate industrial parts in a layer by layer fashion. Despite its great promise in fabrication flexibility, print quality has long been a major barrier for its widespread implementation. Traditional offline post-manufacturing inspections to detect the defects in finished products are expensive and time-consuming and thus cannot be applied in real-time monitoring and control. In-situ monitoring methods by relying on the in-process sensor data, on the other hand, can provide viable alternatives to aid with the online detection of anomalies during the process. Given the crucial importance of melt pool characteristics to the quality of final products, this paper provides a framework to process the melt pool images by a configuration of Convolutional Auto-Encoder (CAE) neural networks. The network's corresponding bottleneck layer learns a deep yet low-dimensional representation from melt pools while preserving the spatial correlation and complex features intrinsic in the images. As opposed to the manual annotation of data by X-ray imaging or destructive tests, an agglomerative clustering algorithm is applied to these representations to automatically extract the anomalies and annotate the data accordingly. A control charting scheme based on Hotelling's T^2 and S^2 statistics is then developed to monitor the process's stability by keeping track of the learned representations and residuals obtained from the reconstruction of original images. Testing the proposed methodology on the collected data from an experimental build demonstrates that the method can extract a set of complex features that are inextricable otherwise by using hand-crafted feature engineering methods. Moreover, through extensive numerical studies, it is shown that the proposed feature extraction and statistical process monitoring scheme is capable of detecting the anomalies in real-time with accuracy and F_1 score of about 95% and 82%, respectively.

1. Introduction

Additive manufacturing consists of successive fabrication of materials layer upon layer to manufacture three-dimensional items. There are diverse categories of additive manufacturing processes, including Sheet Lamination Processes (SLP), Binder Jetting Processes (BJP), Extrusion-Based processes (EBP), Material Jetting Processes (MJP), Photo-polymer Vat Processes (PVP), Powder Bed Fusion (PBF), and Directed Energy Deposition (DED) [1–3]. In a variation of PBF called Laser Powder Bed Fusion (LPBF), laser power is utilized to melt and fuse the spread powder on a build plate. An LPBF machine can precisely scan thin layers of powder to form a designed geometry. The laser delivers thermal energy to the powder to create melt pools once it reaches the melting temperature. Developments of porosity and keyholing due to lack of fusion and over melting phenomena, respectively, are two key factors that significantly deteriorate the material properties of finished products [4–6]. Moreover, it has been proven through extensive studies that the different morphological characteristics of the melt pool region are closely correlated to the formation of such defects on parts [7–9]. The formation of melt pool regions can get affected by several exogenous and environmental factors such as fluid dynamics, thermal conduction, and preheating temperature. Nonetheless, the process parameter settings play a primary role in controlling the process and forestalling defects and anomalies. Laser power, scan velocity, and hatching distance are the primary energy density related variables that can be leveraged to alter the formation of the melt pool [10,11].

* Corresponding author.
E-mail addresses: Sepehr.Fathi@asu.edu (S. Fathizadan), Feng.Ju@asu.edu (F. Ju), yan.lu@nist.gov (Y. Lu).
[1] This work is supported by Department of Commerce under grant 70NANB20H194.

https://doi.org/10.1016/j.addma.2021.101961
Received 11 November 2020; Received in revised form 29 January 2021; Accepted 15 March 2021
Available online 5 April 2021

The primary source of investigating the melt pool is captured through acquisition of thermal or optical melt pool images taken in-situ from the laser-powder interface when the laser beam is applied on the powder bed. In general, two post-build approaches correlate a melt pool image to either a normal or defective location/spot on the part: (1) non-destructive inspection by CT-scan X-ray imaging, and (2) destructive inspection [12,13]. Due to the large number of images, obtaining these labels for melt pool images with either approach comes at a great price. The results, in addition, suffer significantly from low accuracy. One can utilize the fact that oversized, small, splashed, or deformed melt pools indicate morphological signatures of defects in parts. Therefore, the objective could be redirected toward detecting the occurrence of such anomalies in the melt pool images. This gives rise to a cheaper yet effective alternative to the manual annotation of data by striving to annotate the data based on the proximity in their corresponding structural properties. The structural properties of the data are captured through a set of high-quality features from samples.

The state-of-the-art methods often rely on oversimplified and hand-crafted features of the melt pool to analyze the images [10,14]. These methods fail to preserve the spatial correlation within images and lose the valuable and intricate information inside each sample. This paper provides a framework to process the melt pool images by a configuration of Convolutional Auto-Encoder (CAE) neural networks. The network's corresponding bottleneck layer learns a deep low-dimensional representation from melt pools while preserving the spatial correlation and complex features intrinsic in the images. As opposed to the manual annotation of data by X-ray imaging or destructive tests, an agglomerative clustering algorithm is applied to these representations to automatically extract the anomalies and annotate the data accordingly. A control charting scheme based on Hotelling's T^2 and S^2 statistics is then developed to monitor the process's stability by keeping track of the learned representations and residuals obtained from the reconstruction of original images. An experimental build using a spiral concentrating scan pattern with varying laser power was conducted on the Additive Manufacturing Metrology Test bed at the National Institute of Standards and Technology (NIST) [15]. Testing the proposed methodology on the collected data demonstrates that the method can extract a set of complex features that are inextricable by using hand-crafted feature engineering methods. Finally, through extensive numerical studies, it is shown that the proposed feature extraction and statistical process monitoring scheme is capable of detecting the anomalies in real-time with relatively high accuracy.

In what follows, we first discuss an overview of relevant studies in Section 2. The proposed pipeline to process and analyze the melt pool images, including convolutional auto-encoder for deep representation learning, agglomerative clustering for data annotation, and statistical process control for anomaly detection, will be explained in Section 3. The proposed methods will be evaluated by an experimental build. The experiment settings and the numerical results will be provided in Section 4. Finally, conclusions and future directions are outlined in Section 5.

2. Literature review

Overall, the literature in characterizing and analyzing melt pool images is divided into three different categories: parametric modeling, non-parametric modeling, and deep learning. Concerning parametric analysis, Yang et al. predict the melt pool area by considering laser power, scan velocity, and tool-path on multiple track geometry as the predictor variables [10]. First, different rectangular parts with different path strategies are printed. Using different thresholding values on melt pool images, the area of the fitted ellipse is extracted. Finally, taking the spatio-temporal effects of neighboring melt locations into account, a polynomial regression model named "neighboring-effect modeling method" (NBEM) is developed and fitted on the data. In a later study, Yang et al. develop a new model called Layer-wise NBEM (L-NBEM) by further including the scan and exposure settings data from the previous layers [10]. Unlike previous work, a fully-connected neural network is trained on the data with a new set of features to predict the melt pool area. Given the spatio-temporal interdependence of data, Guo et al. develop a framework to model and monitor the melt pool [16]. Following the general linear mixed models, a Spatio-Temporal Conditional Auto-Regressive (STCAR) model is deployed to account for both spatial correlations among pixels in an image and temporal correlations across images. A Statistical Process Control (SPC) scheme based on Hotelling T^2 statistics is then used to monitor the estimated parameters from the model over time.

Several studies characterize the data by non-parametric modeling approaches. Khanzadeh et al. propose a framework to predict (detect) porosity based on thermal images from the melt pool [17]. They characterize the melt pool images by transforming the data into a spherical coordinate system and applying bi-harmonic surface interpolation afterward to smoother and extract the vector of features. These vectors are later put into Self-Organizing Maps (SOM) to cluster each image to decide whether it is normal or porous. A CT-scan X-ray imaging system capable of accurately identifying the sizes and locations of pores is used to benchmark the model's performance. A very similar work of study is done by Khanzadeh et al. [18], where instead of thermal, the morphological characteristics of the melt pool image are extracted and used for analysis. Specifically, the data points belonging to the melt pool boundary are transformed into the polar coordinate system, and cubic spline is used to serve the purpose of smoothing and feature extraction. Another similar example of research conducted by Khanzadeh et al., uses Functional Principal Component Analysis (FPCA) to obtain the morphological features from melt pool images and classifies each image as normal or porous using different classification algorithms such as Support Vector Machines (SVM) and Decision Trees (DT) [19]. In another effort to preserve the spatio-temporal characteristics of the melt pool images, Khanzadeh et al. develop an SPC approach using Hotelling T^2 and Q charts, that monitors the extracted features from the decomposition of tensor data [20]. The obtained accuracy and F_1 score measures from this approach are highly volatile due to the large standard deviations of the results.

Following the same stream of research, Grasso et al. unfold the tensor of streams of optical melt pool images to obtain a vectorized form for each pixel across the layers [21]. Using Vectorized Principal Component Analysis (VPCA), a set of weights and Hotelling's T^2 distances are assigned to each frame and each pixel, respectively. Finally, the vanilla k-means clustering is utilized to monitor the process. Grasso et al. perform several image processing tasks, including image segmentation by Otsu and contour detection, to extract the melt pools from infrared images [22]. The statistical descriptors to be controlled are the average thermal intensity of all retrieved pixels and the melt pool area defined based on the number of pixels in the detected contour. A bi-variate control charting scheme based on Hotelling T^2 is then developed to monitor the melt pool's stability over time. Gobert et al. conduct another study with the aim of binary classification of voxels from layerwise optical images collected during build-time [12]. Feature extraction is done by applying $3D$ convolution filters on the data from multiple modalities. On the other hand, the x, y, z locations of porosity are detected by the convolution of a Gaussian kernel with CT images. Finally, the outputs from single classifiers trained on each modality are concatenated to vote for the porosity decision. The best resultant approximate accuracy and F_1 score are reported to be about 85% and 62%, respectively.

As discussed above, the state-of-the-art methods often rely on handcrafted feature engineering methods to characterize the melt pool area. For instance, a few morphological or thermal attributes can be derived and considered as features. A few methods make an effort to take the spatio-temporal characteristics of the process into account. After the feature engineering phase, statistical monitoring methods or different machine learning tasks such as clustering or classifications can be defined to monitor the process's stability and detect/predict

anomalies. Recently, another field of data-driven modeling has emerged, which can potentially surpass the previous methods that rely on humans to extract the features. This is realized by interlacing the feature extraction with learning mechanism [23]. Thus, more smart models are developed that can automatically extract and incorporate high-quality features and therefore gain superior performance over machine learning methods.

The employment of deep learning methods within the additive manufacturing domain is still in a very preliminary stage. Among the handful of studies, Kwon et al. utilize the Convolutional Neural Networks (CNN) to build a regression model to predict the laser power values from melt pool images [24]. This method accounts for spatial correlation within the images but fails to address the temporal correlation across images. In another very similar study, Zhang et al. perform a set of image processing steps such as Otsu thresholding and feature matching to process the cross-sectioning and CT images to extract the size and location of pores [13]. This information is then used to annotate the melt pool images. Finally, CNN is trained on the data to perform both classification to detect the location of pores and regression to estimate the size of porous regions. This study follows the same stream of research with a focus on extracting features based on learning a deep representation from melt pool images. In doing so, this work offers much broader flexibility in further analysis of the data and anomaly detection than crude classification or regression tasks pursued in the existing studies.

3. Methodology

The framework of the proposed methodology is illustrated in Fig. 1. The pre-processed tensor of melt pool images are fed to the CAE, and the bottleneck tensor from latent space is extracted. This encoded deep representation tensor is then flattened and deployed by a method of agglomerative clustering to annotate the data as either normal or anomaly. In the next step, the CAE is retrained on the normal samples, and the new set of extracted encoded vectors are used to construct the phase-I of the proposed multivariate control charting method. The deep representations of the set of previously discovered anomalies are then employed by the phase-II control charting to evaluate the method's performance in terms of anomaly detection. The three constituents of the framework, including CAE neural networks to process the melt pool images, agglomerative clustering algorithm to annotate the data, and the control charting scheme to monitor the process's stability and perform anomaly detection, are delineated by the next subsections, respectively.

3.1. Deep representation learning for feature extraction from melt pool images

Assume a set of N gray-scale images each with a dimension of $d_1 \times d_2$ and let's denote the flattened vector of i^{th} image by $\overrightarrow{x_i} \in \mathbb{R}^{1\times P}$, for $i = 1, 2, \ldots, N$, where $P = d_1 \times d_2$. The vector of weights associated with each neuron j in the hidden layer is represented by $\overrightarrow{\alpha_j} = [\alpha_{j1}, \alpha_{j2}, \ldots, \alpha_{jP}]$, for $j = 1, 2, \ldots, M$, where M is the total number of neurons in the hidden layer. Furthermore, let $\overrightarrow{\beta_k} = [\beta_{k1}, \beta_{k2}, \ldots, \beta_{kM}]$ be the vector of weights associated with each neuron k in the final output layer, for $k = 1, 2, \ldots, K$, where K is the total number of neurons in the hidden layer or equivalently the number of classes. The output of each output unit k for the input i, $\hat{y}_{ik}$, is the probability of assigning each input vector $\overrightarrow{x_i}$ to class k. The model utilizes the outputs $\hat{y}_{ik}$ to benchmark its performance against y_{ik}, the ground truth for the sample inputs. The criteria for benchmarking is given by a loss function, which is pursued to minimized. Table 1 provides the expression forms of the minimization of two common loss functions, mean squared error and cross entropy.

Table 1
Common loss functions for training neural networks.

	Loss function	
	Mean squared error	Cross entropy
Expression form	$\min_{\alpha,\beta} \frac{1}{N}\sum_{i=1}^{N}\sum_{k=1}^{K}(y_{ik}-\hat{y}_{ik})^2$	$\min_{\alpha,\beta} -\frac{1}{N}\sum_{i=1}^{N}\sum_{k=1}^{K} y_{ik} ln(\hat{y}_{ik})$

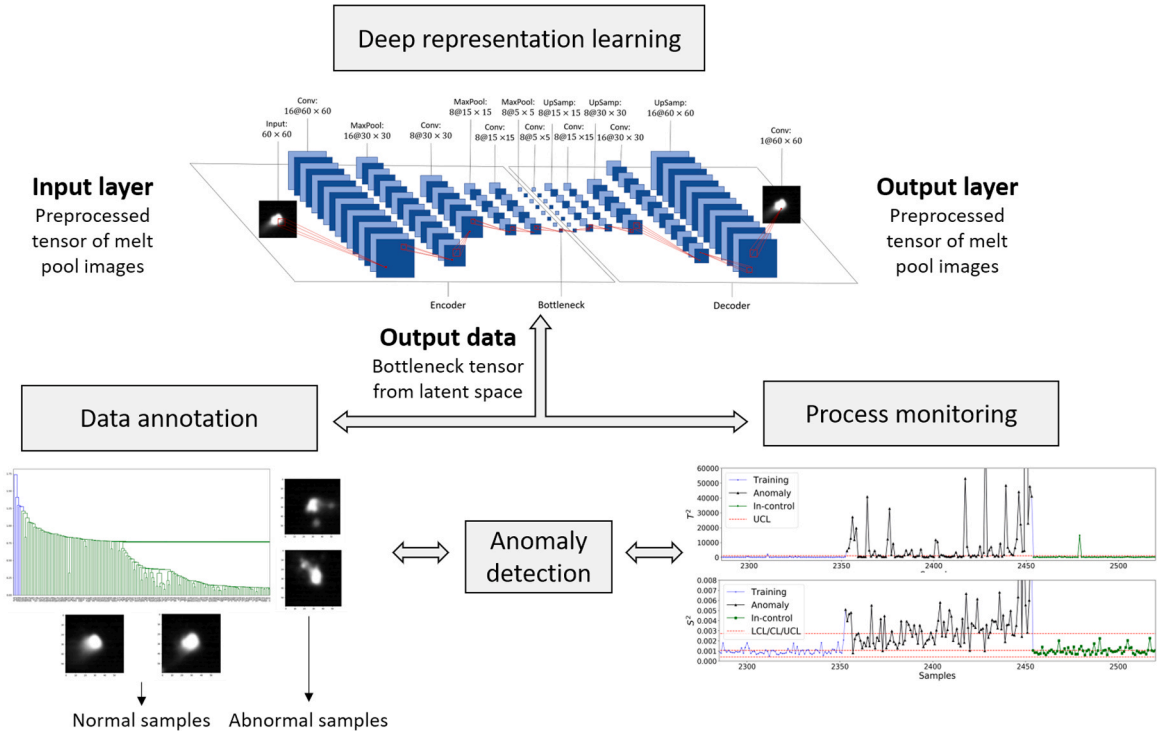

Fig. 1. Framework of proposed deep representation learning for anomaly detection methodology.

Stochastic gradient descent is used to train the neural network on large data sets. Without the loss of generality, consider the loss function after dropping the $1/N$. Denoted by $\mathscr{L}(x;\alpha,\beta)$, it is comprised of sum of errors for each sample, i.e. $\mathscr{L}(x;\alpha,\ \beta) = \sum_{i=1}^{N}\mathscr{L}(x_i;\alpha,\ \beta)$, where $\mathscr{L}(x_i;\alpha,\beta)$ is equal to $\sum_{k=1}^{K}\left(y_{ik}-\hat{y}_{ik}\right)^2$ or $\sum_{k=1}^{K}y_{ik}ln(\hat{y}_{ik})$ in case of mean squared error or cross entropy, respectively. Then, given the weights at time τ, the updated weights at time $\tau+1$ can be found by moving in the direction of the negative gradient. The size of the movement is a small non-negative number called learning rate, and is denoted by γ. Specifically, $\overrightarrow{\alpha}_j$ and $\overrightarrow{\beta}_k$ weights are updates as follows:

$$\begin{bmatrix}\alpha_{j1}^{\tau+1}\\ \vdots\\ \alpha_{jp}^{\tau+1}\\ \vdots\\ \alpha_{jP}^{\tau+1}\end{bmatrix} = \begin{bmatrix}\alpha_{j1}^{\tau}\\ \vdots\\ \alpha_{jp}^{\tau}\\ \vdots\\ \alpha_{jP}^{\tau}\end{bmatrix} - \gamma\begin{bmatrix}\frac{\partial\mathscr{L}(x_i;\alpha,\beta)}{\partial\alpha_{j1}^{\tau}}\\ \vdots\\ \frac{\partial\mathscr{L}(x_i;\alpha,\beta)}{\partial\alpha_{jp}^{\tau}}\\ \vdots\\ \frac{\partial\mathscr{L}(x_i;\alpha,\beta)}{\partial\alpha_{jP}^{\tau}}\end{bmatrix}, \begin{bmatrix}\beta_{k1}^{\tau+1}\\ \vdots\\ \beta_{km}^{\tau+1}\\ \vdots\\ \beta_{kM}^{\tau+1}\end{bmatrix} = \begin{bmatrix}\beta_{k1}^{\tau}\\ \vdots\\ \beta_{km}^{\tau}\\ \vdots\\ \beta_{kM}^{\tau}\end{bmatrix} - \gamma\begin{bmatrix}\frac{\partial\mathscr{L}(x_i;\alpha,\beta)}{\partial\beta_{k1}^{\tau}}\\ \vdots\\ \frac{\partial\mathscr{L}(x_i;\alpha,\beta)}{\partial\beta_{km}^{\tau}}\\ \vdots\\ \frac{\partial\mathscr{L}(x_i;\alpha,\beta)}{\partial\beta_{kM}^{\tau}}\end{bmatrix} \tag{1}$$

The value of partial derivatives of loss of each sample with respect to α_{jp} and β_{km} is computed by the chain rule for derivatives and error backpropagation. The process can be iterated until convergence. Adaptive learning rate and momentum such as "Adam" [25], "Adadelta" [26] and "RMSprop" [27] is used to avoid a local minima. Finally, as the number of samples is relatively large in practice, a batch of samples is used to update the parameters as opposed to one sample at a time procedure in Eq. (1).

The explosion in the number of weights as image data gets large in dimension can lead to excessive computational overheads. Furthermore, there is also a loss in spatial information when images are flattened for the feed forwarding process. As a remedy, Convolution Neural Networks are developed to locally connect the features on the input image to the nodes inside the hidden layers. CNNs consist primarily of three different types of layers: convolutions, pooling, and fully connected layers. Fully connected layers are discussed above, so the details for convolutional and pooling layers are given next. A matrix known as a kernel is slid over the input matrix in the convolutional layers to create a feature map by performing convolution operation [23]. Let K and S be the $f_1 \times f_2$ kernel and feature map matrix, respectively. The feature map can be obtained following the 2-D convolution operation denoted by '*' on the two-dimensional image X as follows:

$$S(i,j) = (X * K)(i,j) = \sum_{m=0}^{f_1-1}\sum_{n=0}^{f_2-1}X(i+m,j+n)K(m,n). \tag{2}$$

Then, a non-linear activation function h such as sigmoid function (σ), hyperbolic tangent (*tanh*), or Rectified Linear Unit (*ReLU*) [28] is applied to the feature map to obtain the final output, i.e., $h(S)$. In practice, more than one kernel is applied to the images so as to extract different types of features. The number of kernels is called filter or kernel depth. Therefore, the final feature map forms a 3D tensor composed of several feature map matrices.

Next, a pooling layer is applied to the feature map produced by the previous layer to downsample the data while preserving spatial invariance. The notion behind pooling layers is relatively straightforward. Max pooling, the most common type of pooling, is to simply take the maximum value from a given array or matrix. In this case, the feature map matrix is partitioned into $w \times u$ submatrices, and the maximum values inside each submatrix are taken to form a new matrix denoted by D:

$$D(i,j) = \max\{S(i+m,j+n)|m \in [0,w], n \in [0,u]\}. \tag{3}$$

It is worth noting that the convolutions and max-pooling layers are stacked on top of each other indefinitely to gain better results in practice.

Finally, the structure behind the proposed CAE can be demystified as follows. Specifically, Auto-Encoders are a method of unsupervised learning that learn a compact representation of the unlabeled input data. As the name suggests, it is composed of two components: an encoder and a decoder. The encoder f learns a mapping from input data X to a compact latent space H, i.e. f: $X \rightarrow H$, and the decoder g that learns a mapping back from latent space to a reconstructed version of original input data $\widetilde{X}$, i.e. $g : H \rightarrow \widetilde{X}$. Remember from above that the ground truth for each sample is represented by $\overrightarrow{y_i} = [y_{i1}, y_{i2}, \ldots, y_{iK}]$, where $y_{ik} = 1$, if sample i belongs to the class k and the rest are simply zero. The Auto-Encoders have exactly the same structure and training process as fully connected neural networks with the difference that $\overrightarrow{y_i}$ is simply replaced with $\overrightarrow{x_i}$. In the case of CAEs, just as similar to CNNs, the data are not flattened, and therefore, the input and output matrices are mapped to each other while the spatial correlation is preserved. The layer which holds the data in the latent space is called the bottleneck layer. The bottleneck layer outputs an encoded tensor of customized dimensions for each X_i denoted by H_i. The model also has several hyper-parameters, including the number of layers, kernel's and pooling's size and depth, that need to be tuned based on cross-validation or test data, as will be discussed in Subsection 4.2.

3.2. Anomaly detection in melt pool images by clustering

The final learned representation vector can be fed to other methods of unsupervised or supervised learning for further analysis. As discussed before, manual annotation of melt pool images is time-consuming and expensive. A variation of clustering algorithms is employed to automatically annotate the melt pool images as either normal or anomaly to tackle this challenge. Anomalies are usually defined as individuals or groups of samples isolated from normal samples by their distinguishable characteristics. Agglomerative clustering tends to merge the samples into clusters in a hierarchical fashion. At the beginning of the process, each sample is a cluster of its own. The children clusters are then sequentially combined by the shortest cophenetic distance (linkage) into larger clusters until all elements end up being in the same parent cluster. An immediate intuition from this procedure is that normal samples tend to merge faster and with shorter cophenetic distances while appending the anomaly samples are postponed until the end of the process and when cophenetic distances between clusters are large. Furthermore, anomalies tend to form singleton clusters of their own, while normal samples are grouped together in clusters with large populations. These characteristics make the agglomerative clustering a perfect candidate for the anomaly detection, and thus automatic annotation of melt pool deep representation flattened vectors.

The definition of linkage is what differentiates between the different agglomerative clustering methods. The most widely used linkage functions include single, complete, average, and Ward. Denote the vectors of flattened encoded tensors by $\overrightarrow{h_i} \in \mathbb{R}^{1\times Q}$, for $i = 1, 2, \cdots, N$, where Q is the product of dimensions of the corresponding tensors. Then, the following linkage functions can be defined:

$$l_{single}(C_i, C_j) = min\{dist(\overrightarrow{h_i}, \overrightarrow{h_j})\Big|\overrightarrow{h_i} \in C_i; \overrightarrow{h_j} \in C_j\}, \tag{4}$$

$$l_{complete}(C_i, C_j) = max\{dist(\overrightarrow{h_i}, \overrightarrow{h_j})\Big|\overrightarrow{h_i} \in C_i; \overrightarrow{h_j} \in C_j\}, \tag{5}$$

$$l_{average}(C_i, C_j) = \sum_{\overrightarrow{h_i}\in C_i}\sum_{\overrightarrow{h_j}\in C_j}\frac{dist(\overrightarrow{h_i}, \overrightarrow{h_i})}{|C_i||C_j|}, \tag{6}$$

$$l_{Ward}(C_i, C_j) = \sqrt{\frac{2|C_i||C_j|}{|C_i| + |C_j|}}, dist\left(\overline{C}_i, \overline{C}_j\right), \tag{7}$$

where $l_k(C_i, C_j)$ denotes the type k linkage between two cluster C_i and C_j. $|C_i|$ is the cardinality of cluster C_i. $\overline{C}_i$ is the centroid of cluster C_i and is computed as $1/\left|C_i\right|\sum_{\overrightarrow{h}_i \in C_i} h_i$. The measure of proximity or similarity between two flattened encoded vectors $\overrightarrow{h_i}$ and $\overrightarrow{h_j}$ is denoted by $dist(\overrightarrow{h_i}, \overrightarrow{h_j})$. The proximity measure also varies in type and include cosine similarity, Manhattan or Euclidean distance, and correlation. For the sake of consistency in computations between different linkage types, Euclidean distance is used as the primary measure of proximity in this study, i.e. $dist(h_i, h_j) = \| \overrightarrow{h_i} - \overrightarrow{h_j} \|_2$. The steps of the agglomerative clustering algorithm are summarized in Algorithm 1. The outputs of the process are summarized by means of a visualization tool called dendrogram, where the hierarchical structure of parent and child clusters are demonstrated by u-shape links. The height of the links in the dendrogram determine the cophenetic distance between two clusters, which can be also used to decide for the best number of clusters and linkage types visually.

Algorithm 1. Hierarchical agglomerative for clustering melt pool images.

1 **Input:** The set of flattened encoded vectors $\{\overrightarrow{h_1}, \overrightarrow{h_2}, \cdots, \overrightarrow{h_N}\}$
2 Type k linkage function $l_k(C_i, C_j)$;
3 **For** $i = 1, \cdots, N$ **do** // loop over the data
4 $C_i = \{\overrightarrow{h_i}\}$; // each object is the cluster of its own
5 **End for**
6 $C = \{C_1, C_2, \cdots, C_n\}$; //super set includes all clusters
7 **While** $|C| > 1$ **do** // loop until super set has only one object
8 $C^*_1, C^*_2 \leftarrow \arg\min\{l_k(C_i, C_j) | C_i \in C; C_j \in C\}$; //pick best clusters to merge
9 $C \leftarrow \{C \backslash C_1^*\} \backslash C_2^*$; // remove them from super set
10 $C \leftarrow C \cup \{C_1^* \cup C_2^*\}$ // add their union to the super set
11 **End while**

$$\overrightarrow{\mu} = \frac{\sum_{i=1}^{N_1} \overrightarrow{h_i}}{N_1}, \tag{9}$$

$$\Sigma = \frac{V^T V}{2(N_1 - 1)}. \tag{10}$$

The computational relationships for i^{th} sample are defined as follows [29]:

$$T_i^2 = [\overrightarrow{h_i} - \overrightarrow{\mu}]^T \Sigma^{-1} [\overrightarrow{h_i} - \overrightarrow{\mu}], \qquad i = 1, 2, \ldots, N_1 \tag{11}$$

The upper control limit for the above statistics given a normal assumption, is approximated using $UCL = \chi^2_{\alpha,Q}$, where $\chi^2_{\alpha,Q}$ is the 100 $(1-\alpha)^{th}$ percentile of chi-squared distribution with Q degrees of freedom. However, as the normal assumption is usually violated in practice, the non-parametric kernel density estimator is fitted on the data to estimate the empirical probability density functions [30,31]. Denote the Gaussian kernel function as $K(u) = \frac{1}{\sqrt{2\pi}} e^{-u^2/2}$ and its bandwidth by b, then the estimated density at point T_i^2 is measured by:

$$\hat{f}(T_i^2; b) = \frac{1}{n}\sum_{j=1}^{N_1} K\left(\frac{T_i^2 - T_j^2}{b}\right), \tag{12}$$

where the optimal value for b is determined by a $K - fold$ cross validation that maximizes the log likelihood of training data. Denote the hold out set at the $k^{th}fold$ by S_k, then the optimal value for b is obtained as follows:

$$b = \arg\max\left(\frac{\sum_{k=1}^{K} \log\prod_{i \in S_k} \hat{f}(T_i^2; b)}{K}\right) \tag{13}$$

The $100(1-\alpha)^{th}$ percentile of the estimated probability density function determines the upper control limit of the control chart.

Note that the flattened encoded vectors store a low-dimensional representation that preserves only the main patterns in the original images. The residual variance of the process can be further investigated to monitor any potential unaccounted variability. The computational relationship for ith sample is calculated as follows:

$$S_i^2 = \frac{\overrightarrow{e}_i^T \overrightarrow{e}_i}{P - 1}, \qquad i = 1, 2, \ldots, N_1 \tag{14}$$

,where the $1 \times P$ vector of the estimated residuals is given by $\overrightarrow{e}_i = \overrightarrow{x_i} - \overrightarrow{\hat{x}}_i$, and $\overrightarrow{\hat{x}}_i$ is the flattened vector of i^{th} decoded image reconstructed from the bottleneck layer. Again, the nonparametric kernel density estimator estimates the empirical probability density function of residual variance statistics. The $100(\alpha/2)^{th}$ and $100(1-\alpha/2)^{th}$ percentiles of the estimated probability density function determine the lower and upper control limit, and $\overline{S^2} = \sum_{i=1}^{N_1} S_i^2 / N_1$ is the central control limit of the control chart, respectively. The two control charts are performing concurrently. Therefore, considering an overall false alarm probability of α, the false alarm probability of each individual control chart can be

3.3. Statistical process monitoring for anomaly detection

As the last step, a multivariate profile monitoring scheme is deployed to perform control charting on the flattened encoded vectors. To this aim, the anomaly images detected by the discussed methods are labeled as out-of-control samples and are discarded out of the phase-I statistical process monitoring where the parameters are estimated, and control limits are built based on normal samples. The anomaly vectors are later employed to evaluate the out-of-control performance of the control charting method. The multivariate profile monitoring scheme consists of a Hotelling's T^2 control chart to monitor the deep representation vectors and a Shewhart control chart for monitoring error variance the of residuals ϵ denoted by σ^2. The first step toward designing the control chart method in phase-I analysis, involves estimating the mean vector, variance-covariance matrix and upper control limits. Denoting the $(N_1 - 1) \times Q$ successive difference matrix by V, it can be calculated as follows:

$$V = \begin{bmatrix} \overrightarrow{v}_1 \\ \overrightarrow{v}_2 \\ \vdots \\ \overrightarrow{v}_{N_1 - 1} \end{bmatrix}, \tag{8}$$

where $\overrightarrow{v_i} = \overrightarrow{h}_{i+1} - \overrightarrow{h_i}$, $i = 1,2,\ldots,N_1 - 1$, and N_1 is total number of normal samples. Then, the variance-covariance matrix Σ and the mean μ are estimated as follows:

determined by $\alpha' = 1 - \sqrt{1-\alpha}$.

4. Case study and results

4.1. Experiment setting

An experiment is conducted on an open-architecture laser powder bed fusion system - the Additive Manufacturing Metrology Testbed (AMMT) at the National Institute of Standards and Technology (NIST) [32]. Fig. 2 illustrates a schematic set up of the testbed with five major subsystems: a build platform, a powder recoating system, a laser positioning optical system, and two process monitoring modules [14]. One of the process monitoring systems is a high-speed camera-based coaxial melt pool monitoring system. The system is designed to allow full control of laser scans as well as synchronized data acquisitions. It uses a real-time controller to set galvo position and laser power as well as trigger the acquisition of melt pool images [33].

In this experiment, a total of 3 × 4 Inconel 625 parts are manufactured on a 100 mm × 100 mm build platform [15]. Each part has the same nominal 10 mm × 10 mm × 5 mm geometry but built with a unique scan strategy - a combination of various scan paths, laser power, and scan velocity. An in-house developed AM software is used to program the scan strategy into a series of position commands with a time interval of 10 μs (100 KHz). The high-speed coaxial melt pool camera is triggered at 2 kHz (500 μs of sample interval). However, the monitoring system only captures melt pool images for one of the 12 parts at each layer due to the camera memory limit. Hence, every part has around 3000 met pool images every other 12 layers.

In this study, part 8 is selected because of its richness of the melt pool characteristics. Fig. 3 shows the scan strategy of this part, named "island spiral concentrating scan strategy". Each layer on the part is composed of four adjacent islands that are printed sequentially. The laser scans each island, spirally following the numbering order shown in the figure. The part has 250 layers, each with 20 μm thickness. The machine reduces the scan speed when the laser turns direction. The machine also reduces the laser power for scan speed to avoid high energy input. Moreover, to avoid high heat concentration and introduce island shape variance, the machine would rotate the centroid angle at each layer. The range of laser power and scan speed is from 0 to 234.83 W and 0–900 mm/s, respectively. Part 8 has melt images captured at layer 8, 20, and 32, etc. We chose the images from layer 8 for the deep representation learning and control chart method validation.

4.2. Deep representation learning of melt pool images

The melt pool images from layer 8 of the process have been collected.

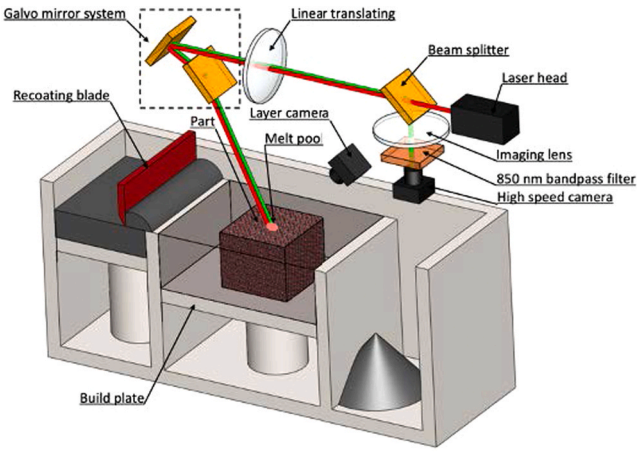

Fig. 2. Schematic of the AMMT experiment setup [14].

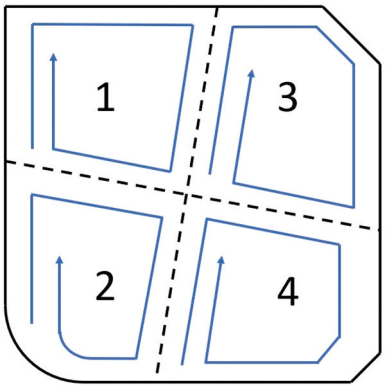

Fig. 3. Schematic of the experimental build and the scan strategy.

The original tensor of the data-set has shape 3769 × 128 × 120, which means there are 3766 total images each with a resolution of 128 × 120. An example of an original image is shown in Fig. 4a. The original images are cropped to the largest common frame that includes the heated area zone's information. The cropped images now have a resolution of 60 × 60, as shown in Fig. 4b. As the last step toward image preprocessing and following the convolution operation in Equation 2, a 2*D* sharpening kernel matrix is slid twice on each image to represent the local features in each image. The example image after the sharpening process is illustrated in Fig. 4c.

Next, the images are randomly split into training and testing data by a proportion of 75% and 25%, respectively. Thus a total of 2824 images are used for training the CAE, and the rest 942 images are utilized to validate the model and prevent potential overfitting. The images are also normalized to have pixel intensities in [0,1] interval before feeding to the CAE. The proposed CAE architecture is comprised of 14 layers, out of which the first and last layers contain the input and output images, respectively. The summary of the model layers, excluding the input and output layers, is shown in Table 2. Layers 2–7 and layers 8–13 in the model form the encoder and decoder, and are represented as '*operation_e#*' and '*operation_d#*', respectively in the table. The compact deep representation from each image is stored in the feature map tensor from the encoder's last layer, i.e., '*MaxPool_e6*'. This layer is called the bottleneck layer. The architecture of the resulting feature map tensors is illustrated in Fig. 5. In the figure, the number of slices and the corresponding dimension for each slice in each layer is shown before and after @ sign, respectively. The deep representation tensor has a dimension of 8 × 5 × 5.

The CAE model is compiled using the following settings: optimizer 'Adadelta' with a batch of size 32, binary cross-entropy as the loss function, and training on 200 epochs. Fig. 6 demonstrates the learning trend for both train and test data resultant from the training process. The y-axis in the figure displays the loss function and x-axis is the number of epoches. Ten arbitrary learned encoded deep representation of melt pool images are obtained from the bottleneck layer, and each is reshaped to a matrix of shape 40 × 5 so that it could be displayed as an image. The third row in Fig. 7 depicts these vectors. Moreover, the first and second row provides the corresponding original images, and decoded images reconstructed using information from the bottleneck layer, respectively. As shown by the figure, the encoded vectors are capable of downsampling the original image while preserving the melt pool's local characteristics. Furthermore, the encoded vectors provide a compact deep representation that can be fed to other methods of supervised or unsupervised learning models for further analysis. For this aim, the encoded tensors of the shape 8 × 5 × 5 are flattened to form 200 × 1 vectors. Therefore the original data set is downsized to a total of 3766 samples, each with 200 features.

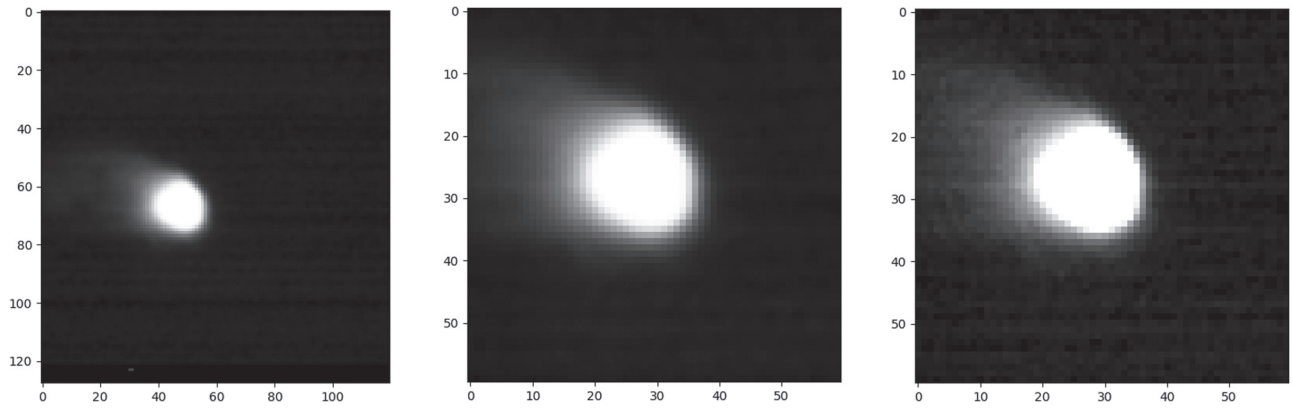

(a) Original image (b) Cropped image (c) Sharpened image after 2*D* convolution

Fig. 4. Image pre-processing on melt pool images.

Table 2
Configuration of the convolutional auto-encoder.

Type	Layer name	Operation	Number of filers	Filter size	Padding
Encoder	*conv2D_e1*	*Convolution + ReLU*	16	3×3	1
	MaxPool_e2	*Maxpooling*	1	2×2	0
	conv2D_e3	*Convolution + ReLU*	8	3×3	1
	MaxPool_e4	*Maxpooling*	1	2×2	0
	conv2D_e5	*Convolution + ReLU*	8	3×3	1
	MaxPool_e6	*Maxpooling*	1	3×3	0
Decoder	*conv2D_d1*	*Convolution + ReLU*	8	3×3	1
	UpSamp_d2	*UpSampling*	1	2×2	0
	conv2D_d3	*Convolution + ReLU*	8	3×3	1
	UpSamp_d4	*UpSampling*	1	2×2	0
	conv2D_d5	*Convolution + ReLU*	16	3×3	1
	UpSamp_d6	*UpSampling*	1	3×3	0

4.3. Anomaly detection by clustering

This step aims to annotate the melt pool images as either normal or anomaly. The hierarchical-based agglomerative clustering with single linkage given by Algorithm 1 was performed on the flattened encoded vectors, and the resulting dendrogram is illustrated in Fig. 8. The x-axis shows the samples, and the y-axis provides the cophenetic distance to merge the clusters sequentially. The dendrogram's visual inspection reveals several parent clusters with their approximate partitionings specified by the vertical dashed lines in the figure. Investigating the images inside each cluster also reveals that they share common characteristics. For instance, the angle of the tail of the melt pools is the same inside each cluster. However, the first and the second clusters display quite different behaviors in the dendrogram. First, the number of samples in the first cluster is low. Second, the samples in this cluster tend to merge at a relatively large cophenetic distance compared to the rest of the samples in the data set, meaning they tend to form the singleton clusters of their own. Lastly, and on the contrary, the samples inside the second cluster are merged at a relatively small cophenetic distance, and their numbers are also large. These points suggest that the data set can be partitioned into three major distinctive clusters: cluster C_1 composed of a few singleton clusters, cluster C_2, and cluster C_3 composed of remaining clusters.

Truncating the dendrogram at the cophenetic distance of 0.70, results in a total of 94 singleton clusters, two doubleton clusters, one tripleton cluster, one cluster with 530 samples, and one cluster with 3138 samples. One can confirm that the 97 singleton and near singleton clusters belong to C_1, the cluster with 530 samples is C_2, and the cluster with 3138 samples is, in fact, C_3. Three arbitrary images inside each of these clusters are selected and displayed in Fig. 9. The left-hand side, middle, and right-hand side panel contain images in C_1, C_2, and C_3 clusters, respectively. From now on, clusters C_1, C_2, and C_3 will be referred to as "anomaly", "noisy", and "normal" clusters, respectively. This also allows for the construction of multi-variate control charting method as described before, after removing the samples inside anomaly and noisy clusters.

4.4. Statistical process monitoring and anomaly detection performance

Given a set of normal melt pool image obtained by the methodologies described in the last subsections, one can proceed to perform a control charting scheme to monitor the stability of the process and also detect

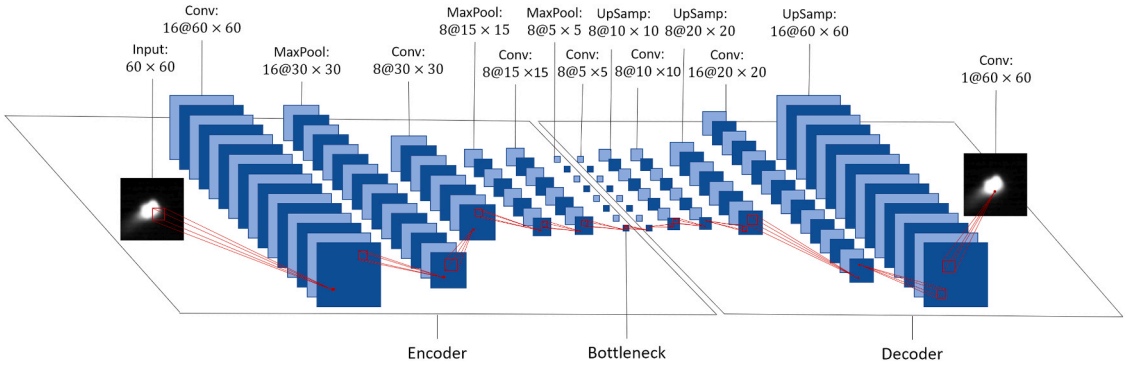

Fig. 5. The architecture of input images, feature map matrices and output images.

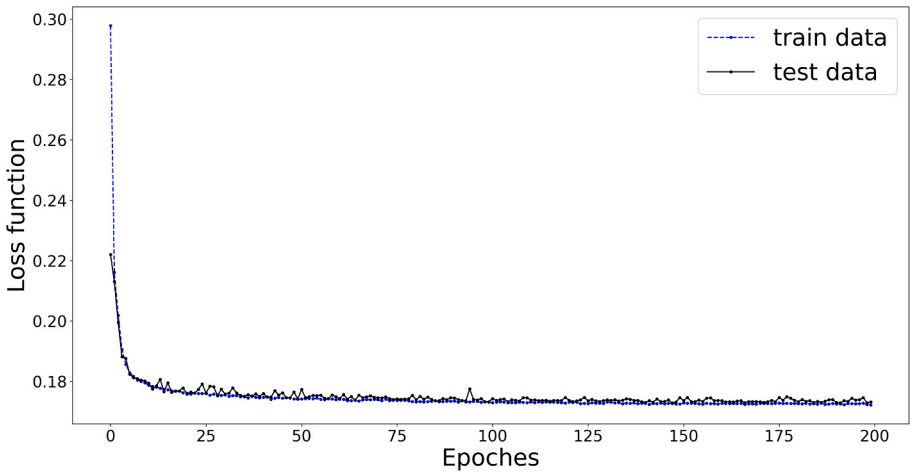

Fig. 6. The train and test learning curves to extract the deep representations from melt pool images.

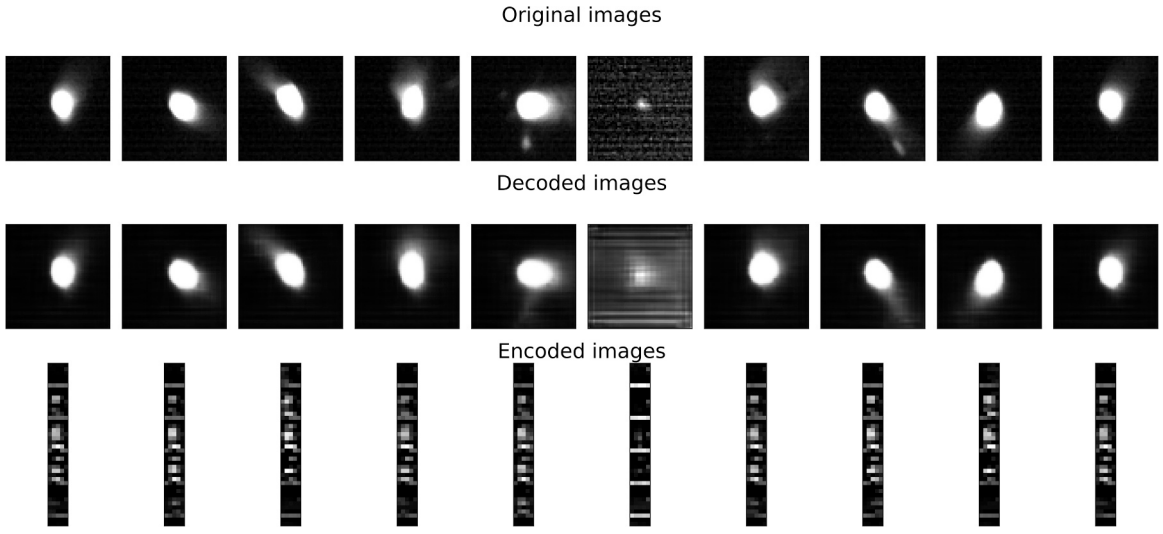

Fig. 7. 10 arbitrary melt pool images.

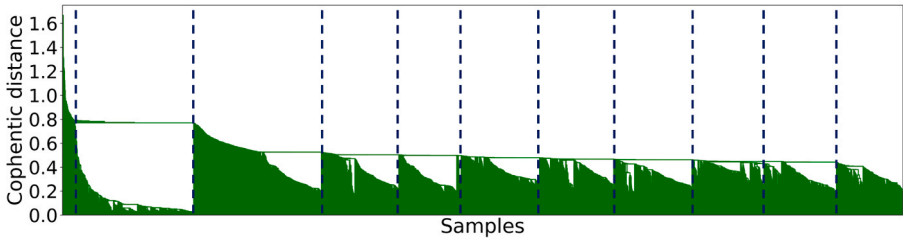

Fig. 8. Dendrogram for hierarchical-based agglomerative clustering with single linkage.

the anomalies and out of control situations in real-time. To this aim, first, the normal data set is randomly split into training and testing sets by a proportion of 75% and 25%, respectively. Then, the same configuration of CAE proposed in Table 2 is retrained and validated this time on the new training and testing data, respectively. Next, the flattened encoded tensors of melt pool images belonging to the training data are used to construct the phase-I control charting scheme proposed in Subsection 3.3. In this phase and in regards to Hotelling's T^2 control chart, the mean vector μ and variance-covariance matrix Σ given by Eqs. (9) and (10) and the value of *UCL* are estimated all based on the training data. *LCL*, *CL*, and *UCL* values pertaining to residual variance monitoring are also estimated using the original and decoded training images.

In phase-II monitoring, the estimated parameters are used to calculate the statistics for monitoring data and decide if the process is either in control or out of control. Basically, a decision for out of control situation is made when either of T^2 or S^2 control charts issue an out of control alarm. This happens when either monitoring statistics exceeds their corresponding control limits. On the other hand, if both statistics

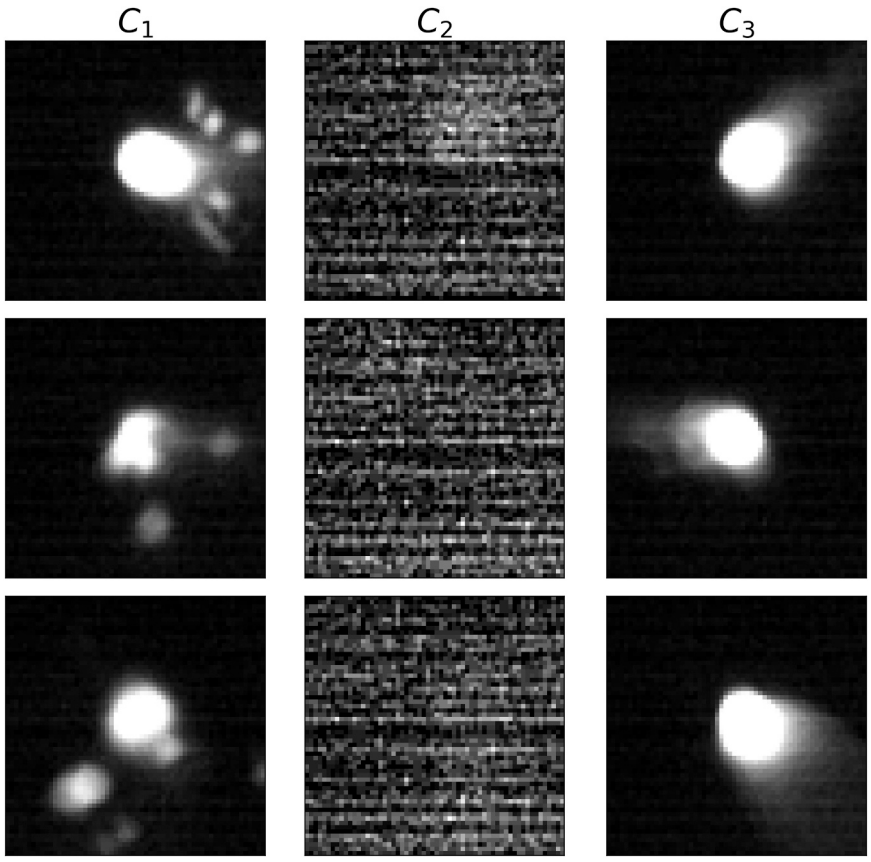

Fig. 9. Sample melt pool images inside C_1:anomaly, C_2:noisy, and C_3:normal clusters.

fall inside the control limits, the process can be considered in control. In order to acquire the monitoring data, the melt pool images in the noisy cluster are all discarded. The testing data and images in anomaly clusters are labeled as "normal" and "anomaly" data, respectively, and their encoded and decoded tensors are obtained by running them through the trained CAE. The former and the latter are then employed to evaluate the control charting method's performance in terms of triggering false alarms and true anomaly detection, respectively. The common practice to this aim involves forming a confusion matrix that stores the values for True Positive (TP), False Positive (FP), True Negative (TN), and False Negative (FN). In the context of the control chart monitoring, a sample can come under one of the following categories:

- *TP*: if it is anomaly and detected as out of control
- *FP*: if it is normal but detected as out of control
- *TN*: if it is normal and detected as in control
- *FN*: if it is anomaly but detected as in control

Using the elements of confusion matrix, a set of criteria are defined as follows to asses the quality of process monitoring:

where *accuracy* measures the ratio of overall true classifications to the number of samples, *specificity* measures the ratio of true classification of normal samples to the number of normal samples, *sensitivity* measures the ratio of true classification of anomalies to the number of anomalies, *precision* measures the ratio of true classification of anomalies to the number of classification of anomalies, and finally $F_1 score$ is the harmonic mean of *sensitivity* and *precision*.

$$Accuracy = \frac{\sum(TP+TN)}{\sum(TP+FP+TN+FN)}, Specificity = \frac{\sum(TN)}{\sum(TN+FP)},$$

$$Sensitivity = \frac{\sum(TP)}{\sum(TP+FN)}, precision = \frac{\sum(TP)}{\sum(TP+FP)}, F_1 score = 2\frac{Sensitivity.Precision}{Sensitivity+Precision},$$

As it was discussed by Section 3.3, the $100(1-\alpha)^{th}$ percentile of the estimated probability density function for measured statistics will be used to determine the control limits. This means there is a 100α probability that the statistics go above the control limits and get detected as out-of-control (rejected) while they are in fact in control (true null hypothesis). The larger the α, the smaller the control limits and thus more alarms will be issued by the charts and vice versa. This will also impact the out-of-control detection power of control charts that is represented by $1-\beta$ error, where β is the probability of accepting a sample while it is out-of-control. It is common to choose the type-I error as a number between 0.001 and 0.05, which means the corresponding control charts will issue false alarm warnings 0.1% and 5% of the time. 10 equally spaced points inside this interval are chosen to test and find the best control limits and therefore the best trade-off between chart's false alarm rate and out-of-control detection power. By selecting 10 different

Table 3
Performance measurement criteria for different training splits and type-I error probability of α'.

Measurement	Type-I error probability of α'									
	0.0010	0.0064	0.0119	0.0173	0.0228	0.0282	0.0336	0.0391	0.0445	0.0500
Accuracy	93.10% (0.0067)	94.58% (0.0040)	95.16% (0.0032)	95.40% (0.0025)	95.38% (0.0035)	95.24% (0.0061)	95.07% (0.0061)	94.87% (0.0060)	94.67% (0.0064)	94.43% (0.0069)
Specificity	99.35% (0.0024)	98.78% (0.0034)	98.30% (0.0034)	97.93% (0.0050)	97.47% (0.0056)	96.99% (0.0076)	96.53% (0.0081)	96.05% (0.0081)	95.63% (0.0082)	95.22% (0.0081)
Sensitivity	47.55% (0.0633)	64.88% (0.0473)	73.79% (0.0467)	78.74% (0.0287)	82.10% (0.0248)	84.68% (0.0301)	86.76% (0.0199)	88.74% (0.0194)	90.22% (0.0179)	91.31% (0.0138)
Precision	92.93% (0.0322)	90.00% (0.0283)	87.47% (0.0220)	85.74% (0.0326)	83.34% (0.0329)	81.02% (0.0405)	78.92% (0.0391)	76.87% (0.0371)	75.19% (0.0361)	73.57% (0.0344)
F_1score	62.64% (0.0567)	75.24% (0.0287)	79.91% (0.0234)	81.99% (0.0100)	82.63% (0.0118)	82.70% (0.0216)	82.57% (0.0190)	82.30% (0.0179)	81.95% (0.0190)	81.44% (0.0212)

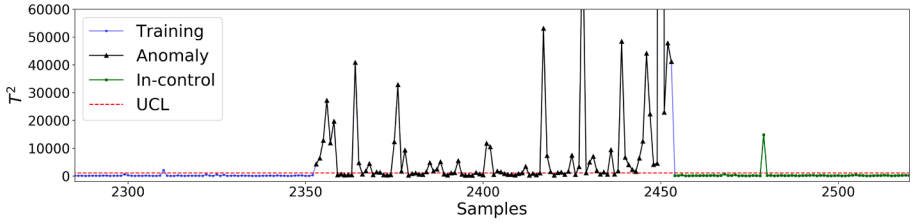

(a) Hotelling's T^2 control chart to monitor the flattened encoded vectors

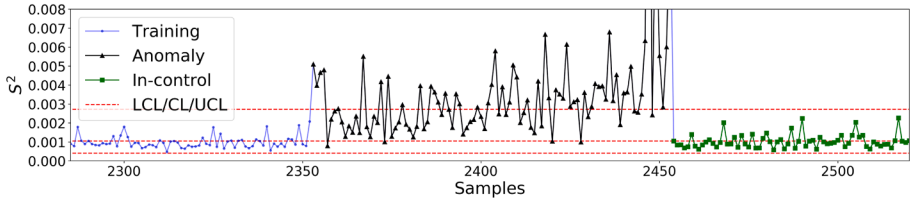

(b) S^2 control charts to monitor the variance of residuals

Fig. 10. Anomaly detection by statistical process monitoring on top of the convolutional auto-encoders.

random proportions of the data from the normal cluster as training data for each of the control chart configuration, 100 trials were conducted. Table 3 provides the results for performance measurements criteria. The standard deviation of results is given in parenthesis below each entry. The highest scores for each measurement have been emboldened in the table. All the measurements are either monotonically increasing or decreasing with respect to α', except for *accuracy* and F_1*score* that reach their maximum at $\alpha' = 0.0228$. On rare occasions where the true classification of normal samples is preferable to the practitioner, the high score of *Specificity* can be used to select the α'. Fig. 10 illustrates a slice of phase-II T^2/S^2 control charting scheme constructed based on $\alpha' = 0.0228$. It includes the entire samples from anomalies and covers a portion of training and test data. The data are sorted according to their labels to provide a better visual intuition into the control charting method's performance regarding the true classification of samples.

4.5. Comparison with hand-crafted features

As it can be observed by the right-hand side images in Fig. 9, the deep representation of melt pool images allows for the detection of eccentric types of anomalies that are not detectable by the handcrafted feature engineer methods. For example, two melt pool images might encompass the same amount of bright pixels or share the same melt pool area, but the splashing effect could still distinguish them from each other. The NBEM model [10] described briefly in Section 2 is an example study that uses the area of fitted ellipses on the thresholded images of melt pools as the feature of interest. It should be noted that this work and NBEM study both share the same experiment setting and data set of melt pool images. In order to extract the features according to [10], the threshold value of 150 is chosen to segment the melt pools from surrounding areas.

Similar to the procedure described in Subsection 4.4, normal melt pool images are employed to construct the phase-I control charting and estimate the parameters. However, in this case, a univariate monitoring scheme composed of a I and a MR chart is deployed. The I chart is provided to monitor the individual observations, and their moving range is monitored by the MR chart.[34]. The individual observations represented by x_i are simply the measured melt pool areas, and their moving range can be calculated as $MR_i = |x_i - x_{i-1}|$. The UCL, CL, and LCL for the I chart to monitor x_is is obtained as follows:

$$\begin{aligned} UCL &= \bar{x} + 3\frac{\overline{MR}}{d_2} \\ CL &= \bar{x} \\ LCL &= \bar{x} - 3\frac{\overline{MR}}{d_2}, \end{aligned} \tag{15}$$

where $\bar{x} = \frac{\sum_{i=1}^{N_1} x_i}{N_1}$, $\overline{MR} = \frac{\sum_{i=2}^{N_1} MR_i}{N_1 - 1}$, and d_2 is a predetermined constant equal to 1.128. Moreover, the UCL, CL, and LCL for the MR chart can be obtained as follows:

$$\begin{aligned} UCL &= D_4\overline{MR} \\ CL &= \overline{MR} \\ LCL &= D_3\overline{MR}, \end{aligned} \tag{16}$$

where D_3 and D_4 are predetermined constants equal to 0 and 3.267, respectively. Fig. 11 illustrates the phase-II $I - MR$ control charting scheme constructed based on the above control limits. It includes the entire samples from anomalies and covers the same portion of training and test data as Fig. 10. Similarly, the data are sorted according to their

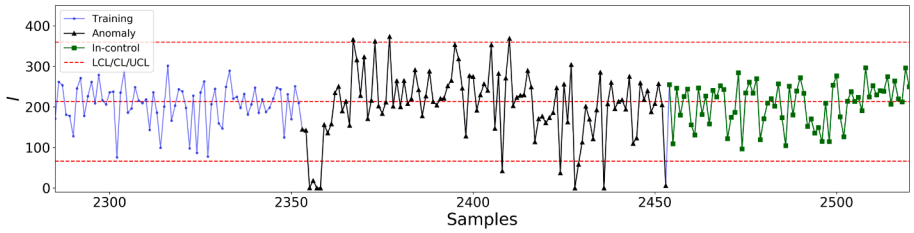

(a) I control chart to monitor the melt pool areas

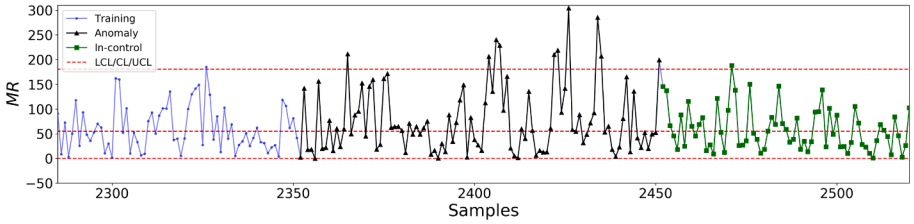

(b) MR control charts to monitor the moving ranges

Fig. 11. Anomaly detection by statistical process monitoring on top of the melt pool areas.

Table 4
Performance measurement criteria comparison between NBEM and proposed method for different training splits.

Model	Accuracy	Specificity	Sensitivity	Precision	F_1score
NBEM	89.20% (0.0045)	98.38% (0.0052)	17.89% (0.0029)	59.77% (0.0798)	27.32% (0.0079)
Deep representation learning	95.38% (0.0035)	97.47% (0.0056)	82.10% (0.0248)	83.34% (0.0329)	82.63% (0.0118)

label to provide better visualization. As it is obvious by the comparison between the two figures, the control charting scheme based on the proposed deep representation learning approach outperforms the method based on melt pool areas in terms of anomaly detection. The set of performance measurement criteria was calculated for 100 trials, and the results are provided in the first row of Table 4. The second row in the table provides the results based on $\alpha' = 0.0228$ for the proposed deep representation learning method. The low values for performance measurement criteria, especially *sensitivity*, *precision*, and $F_1 score$ compared to the proposed method, prove that simple characterization of melt pools by their area results in losing valuable information vital to maintaining a quality process monitoring and control.

5. Conclusions

Sensor data, including melt pool images, carry the most important signatures of the Laser Powder Bed Fusion (LPBF) process and other additive manufacturing technologies. Data-driven in-situ process monitoring and control methods mine this information to shed light on the correlation between process parameter settings and quality characteristics of interest without accounting for the actual physics-based modeling. While the state-of-the-art methods often rely on hand-crafted feature engineering methods to extract a set of features from sensor data, this paper developed a methodology to gain a set of smart features that provide a more in-depth description of the data. Specifically, a configuration of Convolutional Auto-Encoder (CAE) neural networks processes the collected melt pool images to learn a low-dimensional but deep representation from data. The extracted features are plugged into an agglomerative clustering algorithm to tag the anomalies and automatically annotate the data due to the burdensome and expensive manual annotation process. Subsequently, a Hotelling's T^2 and S^2 control charting scheme is developed to monitor the process's stability by keeping track of the learned representations and residuals obtained from the reconstruction of original images. Finally, the numerical results from a real-world case study are provided to prove the proposed method's effectiveness, applicability, and accuracy. The frequency of data acquisition is usually high, resulting in a large volume of data. Therefore, in addition to the spatial correlation within each sample, it is also important to account for the temporal interrelation between samples. Future studies can be directed toward investigating deep learning techniques for time series analysis by considering instances as sequences of samples. Furthermore, this study examined the detection of anomalies in real-time. It is also worth studying the incorporation of control methods to the model and optimize the process parameter settings to ensure certain targets for the quality characteristics are met online.

Declaration of Competing Interest

The authors declare that they have no known competing financial interests or personal relationships that could have appeared to influence the work reported in this paper.

References

[1] I. Astm, Astm52900–15 Standard Terminology for Additive Manufacturing–general Principles–terminology, ASTM International, West Conshohocken, PA, vol.3, no.4, p.5, 2015.
[2] F. Wang, S. Fathizadan, F. Ju, K. Rowe, N. Hofmann, Print surface thermal modeling and layer time control for large-scale additive manufacturing, IEEE Trans. Autom. Sci. Eng. (2020).
[3] S. Fathizadan, F. Ju, K. Rowe, N. Hofmann, A. Fiechter, A novel real-time thermal analysis and layer time control framework for large scale additive manufacturing, J. Manuf. Sci. Eng. (2020).
[4] W.E. Frazier, Metal additive manufacturing: a review, J. Mater. Eng. Perform. 23 (6) (2014) 1917–1928.
[5] H. Gong, K. Rafi, H. Gu, T. Starr, B. Stucker, Analysis of defect generation in ti-6al-4v parts made using powder bed fusion additive manufacturing processes, Addit. Manuf. 1 (2014) 87–98.
[6] M. Sadowski, L. Ladani, W. Brindley, J. Romano, Optimizing quality of additively manufactured inconel 718 using powder bed laser melting process, Addit. Manuf. 11 (2016) 60–70.
[7] M. Tang, P.C. Pistorius, J.L. Beuth, Prediction of lack-of-fusion porosity for powder bed fusion, Addit. Manuf. 14 (2017) 39–48.

[8] R. Cunningham, S.P. Narra, C. Montgomery, J. Beuth, A. Rollett, Synchrotron-based x-ray microtomography characterization of the effect of processing variables on porosity formation in laser power-bed additive manufacturing of ti-6al-4v, JOM 69 (3) (2017) 479–484.
[9] S.A. Khairallah, A.T. Anderson, A. Rubenchik, W.E. King, Laser powder-bed fusion additive manufacturing: physics of complex melt flow and formation mechanisms of pores, spatter, and denudation zones, Acta Mater. 108 (2016) 36–45.
[10] Z. Yang, Y. Lu, H. Yeung, S. Krishnamurty, From scan strategy to melt pool prediction: a neighboring-effect modeling method, J. Comput. Inf. Sci. Eng. 20 (2020) 5.
[11] J. Ciurana, L. Hernandez, J. Delgado, Energy density analysis on single tracks formed by selective laser melting with cocrmo powder material, Int. J. Adv. Manuf. Technol. 68 (5–8) (2013) 1103–1110.
[12] C. Gobert, E.W. Reutzel, J. Petrich, A.R. Nassar, S. Phoha, Application of supervised machine learning for defect detection during metallic powder bed fusion additive manufacturing using high resolution imaging, Addit. Manuf. 21 (2018) 517–528.
[13] B. Zhang, S. Liu, Y.C. Shin, In-process monitoring of porosity during laser additive manufacturing process, Addit. Manuf. 28 (2019) 497–505.
[14] Z. Yang, Y. Lu, H. Yeung, S. Krishnamurty, Investigation of deep learning for real-time melt pool classification in additive manufacturing, in: Proceedings of the 2019 IEEE 15th International Conference on Automation Science and Engineering (CASE), 640–647, IEEE, 2019.
[15] B. Lane, H. Yeung, Process monitoring dataset from the additive manufacturing metrology testbed (ammt): three-dimensional scan strategies, J. Res. Natl. Inst. Stand. Technol. 124 (2019) 1–14.
[16] S. Guo, W.G. Guo, L. Bian, Hierarchical spatial-temporal modeling and monitoring of melt pool evolution in laser-based additive manufacturing, IISE Trans. (2019) 1–34.
[17] M. Khanzadeh, S. Chowdhury, M.A. Tschopp, H.R. Doude, M. Marufuzzaman, L. Bian, In-situ monitoring of melt pool images for porosity prediction in directed energy deposition processes, IISE Trans. 51 (5) (2019) 437–455.
[18] M. Khanzadeh, L. Bian, N. Shamsaei, S.M. Thompson, Porosity detection of laser based additive manufacturing using melt pool morphology clustering, Solid Free. Fabr. (2016) 1487–1494.
[19] M. Khanzadeh, S. Chowdhury, M. Marufuzzaman, M.A. Tschopp, L. Bian, Porosity prediction: supervised-learning of thermal history for direct laser deposition, J. Manuf. Syst. 47 (2018) 69–82.
[20] M. Khanzadeh, W. Tian, A. Yadollahi, H.R. Doude, M.A. Tschopp, L. Bian, Dual process monitoring of metal-based additive manufacturing using tensor decomposition of thermal image streams, Addit. Manuf. 23 (2018) 443–456.
[21] M. Grasso, V. Laguzza, Q. Semeraro, B.M. Colosimo, In-process monitoring of selective laser melting: spatial detection of defects via image data analysis, J. Manuf. Sci. Eng. 139 (2017) 5.
[22] M. Grasso, A. Demir, B. Previtali, B. Colosimo, In situ monitoring of selective laser melting of zinc powder via infrared imaging of the process plume, Robot. Comput. Integr. Manuf. 49 (2018) 229–239.
[23] I. Goodfellow, Y. Bengio, A. Courville, Deep learning, MIT Press, 2016.
[24] O. Kwon, H.G. Kim, M.J. Ham, W. Kim, G.-H. Kim, J.-H. Cho, N.I. Kim, K. Kim, A deep neural network for classification of melt-pool images in metal additive manufacturing, J. Intell. Manuf. 31 (2) (2020) 375–386.
[25] D.P. Kingma J. BaAdam: A Method for Stochastic Optimization, arXiv preprint arXiv:1412.6980, 2014.
[26] M.D. Zeiler, Adadelta: an Adaptive Learning Rate Method, arXiv preprint. 2012. http://arXiv.org/abs/arXiv:1212.5701.
[27] T. Tieleman, G. Hinton, Lecture 6.5-rmsprop: divide the gradient by a running average of its recent magnitude, Coursera: Neural Netw. Mach. Learn. 4 (2) (2012) 26–31.
[28] C.M. Bishop, Pattern Recognition and Machine Learning, Springer, 2006.
[29] J.D. Williams, W.H. Woodall, J.B. Birch, Statistical monitoring of nonlinear product and process quality profiles, Qual. Reliab. Eng. Int. 23 (8) (2007) 925–941.
[30] E. Martin, A. Morris, Non-parametric confidence bounds for process performance monitoring charts, J. Process Control 6 (6) (1996) 349–358.
[31] S. Fathizadan, S.T.A. Niaki, R. Noorossana, Using independent component analysis to monitor 2-d geometric specifications, Qual. Reliab. Eng. Int. 33 (8) (2017) 2075–2087.
[32] Nist Additive Manufacturing Metrology Testbed. https://www.nist.gov/el/ammt-temps.
[33] B. Lane, S. Mekhontsev, S. Grantham, M. Vlasea, J. Whiting, H. Yeung, J. Fox, C. Zarobila, J. Neira, M. McGlauflin, et al., Design, developments, and results from the nist additive manufacturing metrology testbed (ammt), in: Proceedings of the Solid Freeform Fabrication Symposium, Austin, TX, 1145–1160, 2016.
[34] D.C. Montgomery, Introduction to Statistical Quality Control, John Wiley & Sons, 2007.